Strength-Ductility Behaviour of Al-Si-Cu-Mg Casting Alloys in T6 Temper

C. H. Cáceres,† I. L. Svensson*‡, J. A. Taylor
CRC for Cast Metals Manufacturing (CAST), Division of Materials Engineering, School of Engineering, The University of Queensland, Brisbane QLD 4072 Australia

A comparative study of the mechanical properties of 20 experimental alloys has been carried out. The effect of different contents of Si, Cu, Mg, Fe and Mn, as well as solidification rate, has been assessed using a strength-ductility chart and a quality index-strength chart developed for the alloys.

The charts show that the strength generally increases and the ductility decreases with an increasing content of Cu and Mg. Increased Fe (at Fe/Mn ratio 0.5) dramatically lowers the ductility and strength of low Si alloys. Increased Si content generally increases the strength and the ductility. The increase in ductility with increased Si is particularly significant when the Fe content is high. The charts are used to show that the ductility of strong alloys. The (Cu + Mg) content (at.%), which determines the precipitation strengthening and the volume fraction of Cu-rich and Mg-rich intermetallics, can be used to select the alloys for given strength and ductility, provided the Fe content stays below the Si-dependent critical level for the formation of pre-eutectic α-phase particles or β-phase plates.

Keywords: Al-Si-Cu-Mg casting alloys; alloy A356; alloy A319; tensile strength; tensile ductility; quality index; damage mechanisms, Fe-rich intermetallics

Introduction

The alloys of the Al-7Si-Mg system, such as A356 alloy, have good castability and high ductility and strength. This, combined with a very low tendency to form casting defects, has made them the most commonly used aluminium alloys for structural castings. However, in applications where ductility is not of prime importance, such as cylinder heads, Cu-containing variants of these alloys have the distinct advantage of increased strength at high temperatures and therefore are becoming increasingly popular. This is despite their tendency to develop porosity and hot cracking.[1–3] Another important consequence of including Cu in the composition is to enable the use of secondary alloys, although, by necessity, the latter leads to increased levels of Fe and other impurities with concomitant effects on the casting and mechanical behaviour.

Numerous works have been published dealing with the formation of the as-cast microstructure[1,2,4–7] as well as with the effect of solution heat treatment[8–11] and aging[4,11–13] on the microstructure and mechanical behaviour of Al-Si-Cu-Mg alloys. However, due to the wide latitude in the nominal chemical composition of these alloys a correspondingly wide range of properties in both the as-cast and heat treated conditions are possible, and much more systematic work is needed to fully characterise the alloy family.

In this work a comparison of the room temperature tensile properties of 20 experimental alloys has been carried out. The alloys were designed to assess the effect of different Si, Cu, Mg and Fe contents (at Mn/Fe ratio of 0.5 for the higher Fe levels). A total of 21 alloys have been compared, including an Al-7Si-0.3Mg alloy (A356) used as a reference. Goals set for the work were, on the one hand, to assess the effect of varying the alloy content on the tensile strength and ductility of the alloys and, on the other, to develop a systematic method of alloy selection based on the observed upper and lower bounds to the mechanical behaviour. Two studies of the same group of alloys on the development of porosity and a preliminary metallographic study on the phases formed have been published elsewhere.[3,14,15]

Materials and experimental methods

Castings were made at Comalco Research and Technical Support. Details of the alloys and casting procedure have already been published.[3,14] Briefly, a binary Al-Si alloy was melted in an electric resistance furnace and Si, Mg and Fe-containing and Mn-containing master alloys were added to obtain the desired compositions. The melt was modified with an Sr-containing master alloy and commercial Ti-B grain refiner was added. The melt was poured at 720 °C after degassing. The measured chemical composition of the alloys is shown in Appendix A, Table A-1. The target alloy compositions, shown in Table A-2, were designed to cover the extremes of the Si, Cu and Mg composition of the Al-Si-Cu-Mg alloy family. The Fe targets of 0.2 and 0.5 wt.% represent typical primary and secondary sourced alloys, respectively, while the addition

* On leave from Mechanical Engineering/Component Technology, School of Engineering S-511 11 Jönköping University, Sweden
† Author for correspondence
e-mail address: c.caceres@minmet.uq.edu.au

Table 1 Fe-, Cu- and Mg-rich phases identified in the solution heat treated alloys[15]

Alloy	Nominal composition	Main phases present
1	4.5Si-1Cu-0.1Mg-0.2Fe-0.0Mn	β-Al_5FeSi
2	4.5Si-1Cu-0.1Mg-0.5Fe-0.25Mn	β-Al_5FeSi α-$Al_{15}(Fe,Mn)_3Si_2$
3	4.5Si-1Cu-0.5Mg-0.2Fe-0.0Mn	π-$Al_8Mg_3FeSi_6$ β-Al_5FeSi
5	4.5Si-4Cu-0.1Mg-0.2Fe-0.0Mn	β-Al_5FeSi θ-Al_2Cu
8	4.5Si-4Cu-0.5Mg-0.5Fe-0.25Mn	β-Al_5FeSi (Q) $Al_5Cu_2Mg_8Si_6$
20	9Si-4Cu-0.5Mg-0.5Fe-0.25Mn	θ-Al_2Cu α-$Al_{15}(Fe,Mn)_3Si_2$
21	7Si-0.3Mg-0.15Fe	β-Al_5FeSi π-$Al_8Mg_3FeSi_6$

of Mn to the alloys with higher Fe content was to effect the transformation of the dominant β-Al_5FeSi phase in Mn-free alloys to the preferred α-$Al_{15}(Fe,Mn)_3Si_2$.

A number of plates were cast for each composition in an invertible resin-bonded sand mould assembly with a heavy chill incorporated at one end, designed to simulate the improved low-pressure casting process.[16] Bars were sectioned from some of the plates at two locations, one close to the chill end of the plate (corresponding to $\sim 25\,\mu$m secondary dendrite arm spacing, SDAS) and another closer to the riser end, (corresponding to SDAS $\sim 50\,\mu$m).

The bars were given a standard[8] solution heat treatment at 505 °C for 8 h, quenched in water at 60 °C and subsequently aged 8 h at 165 °C. Tensile test specimens were machined out of the heat-treated bars, with a cross-section of $3 \times 4\,mm^2$ and 15 mm gauge length. Mechanical testing was carried out in a screw-driven machine at a crosshead speed of 1 mm/min, with a knife-edge extensometer attached. At least 4 bars were tested at each composition. Digital data files of the flow curves were stored for later analysis.

Development of microstructure

The microstructures of Al-Si-Cu-Mg castings alloys are essentially made up of three components, the proportions of which are governed by the alloy composition and solidification conditions. The two main components are primary α-aluminium solid solution phase and Al-Si eutectic. The third component of the microstructure can be broadly termed ''other intermetallics'' and these arise from excess amounts of Mg, Cu, Fe and Mn that cannot be contained in the α-Al solid solution phase. The intermetallics adopt various morphologies and form at various times, prior to, during or after the Al-Si eutectic formation period, and can significantly affect the mechanical properties of the alloys.

The phases observed in the alloys of this study[15] are listed in Table 1. Details are given for only one alloy with high Si content since the Si content did not affect the phases present.

Influence of silicon

The level of Si primarily controls the amount of Al-Si eutectic that forms during solidification. The amount of eutectic expected to form in binary aluminium alloys with Si levels similar to those of the present study, i.e., 4.5, 7.0 and 9.0 wt.% Si, is 27, 50 and 68 vol.%, respectively. The fraction of eutectic in the microstructure has several effects on properties. As the Si content increases, the volumetric shrinkage of the alloy upon solidification decreases, reducing the amount of feeding necessary.[17] It also affects solidification reactions involving Fe.[18]

Influence of copper

Copper is partially soluble in α-Al solid solution with a maximum equilibrium solubility of 5.65 wt.%,[19] although the typical dissolved Cu levels found in as-cast Al-Si-Cu alloys is around 1%. Therefore, for alloys with 1 to 4% copper, Cu-rich intermetallic phases typically form in the microstructure. The main phase is θ (Al_2Cu). The as-cast Al_2Cu solidifies in two forms: one massive or blocky and the other a fine eutectic form. The respective amounts of the two types formed depend on the level of Cu, Fe and Sr in the alloy.[7,20–22] The other copper-containing phase that forms in the presence of Mg is[15,23] $Al_5Cu_2Mg_8Si_6$, often called Q phase, although this usually appears in much smaller amounts than Al_2Cu. Both phases form after the main Al-Si eutectic reaction. Increased copper content appears to result in increased porosity in castings,[3] although the effects above 1% Cu may reach a plateau.[24]

Influence of magnesium

Magnesium is soluble in aluminium up to a maximum of 17.4 wt.% at 450C,[19] however even at the low amounts typically added to Al-Si based foundry alloys, i.e. 0.3 to 0.7 wt.%, some Mg will precipitate as Mg_2Si as a constituent of the Al-Si-Mg_2Si ternary eutectic. The Mg_2Si phase forms with a Chinese script morphology, and upon solution treatment readily dissolves such that Mg enters the solid solution.[25] This Mg can be re-precipitated as highly effective strengthening (MgSi) precipitates[26] during a T6 age-hardening treatment.

The Mg in the alloys under consideration is also capable of forming other phases, such as Q in presence of Cu (mentioned above) and as π-$Al_8Mg_3FeSi_6$ in the presence of Fe.[17] The π phase is more resistant to solution treatment than Mg_2Si especially at high Mg contents (0.5–0.7%) and as such can result in some Mg remaining unavailable for precipitation hardening[27–29] as well as reduced ductility.[30] There are also suggestions that Mg may reduce dimensional stability in Al-Si-Cu alloys during solution treatment.[11]

Influence of iron and manganese

The solubility of iron is very low in aluminium alloys and tends to form intermetallics phases, e.g. β-Al_5FeSi platelets, and, since these are brittle, this tends to decrease the ductility of the as-cast material.[31,32] In the presence of Mg, the π-phase can form with either a script or blocky morphology, often in close association with β plates, possibly as the result of a peritectic reaction.[18] These morphologies are also detrimental to the ductility, but less so than large β platelets. The π-$Al_8Mg_3FeSi_6$ phase is able to partially transform to fine-scale β particles during solution treatment in low Mg content alloys (0.3–0.5%) but is resistant to change at higher Mg contents.[10,29] The β platelets do not change substantially with solution treatment.[10] The β-phase has also been shown to strongly influence porosity formation[33–35] in Al-Si-Cu alloys, especially in regions of marginal casting conditions and at iron levels high enough to promote β formation prior to the Al-Si eutectic.

When Mn is present with iron, there is an increased tendency for the α-$Al_{15}(Fe,Mn)_3Si_2$ Chinese script phase to form.[5,18] The presence of α-phase particles rather than β-platelets improves mechanical properties, particularly ductility.[5,9] This may in part be due to the reduction in shrinkage porosity that α promotes.[36] In general, Mn:Fe ratios of $\sim$0.5 are considered sufficient to promote complete α for β substitution during typical commercial casting conditions, however overall volume fractions of intermetallic phase are increased in this event. The level of Fe at which pre-eutectic α-$Al_{15}(Fe,Mn)_3Si_2$ phase particles or β-Al_5FeSi plates form depends on the Si content.[18] This relationship is crucial for understanding the influence of Fe on the ductility when the Si content is a variable, as in these experiments. This is discussed in more detail in relation to Figs 7 and 8.

Influence of the solidification rate (SDAS)

The finer dendrite arm spacings observed at high solidification rates result in more uniform microstructures with the potential for more closely distributed and finer, smaller particles (eutectic silicon and intermetallics).[1,2,7] Defect sizes, e.g. porosity, are also reduced as SDAS decreases.[1,2,37] The overall effect is an improvement of ductility with reduced SDAS.

Response to ageing

Precipitation hardening of Al-Si-Cu-Mg alloys involves a mixture of phases normally found in Al-Mg-Si, Al-Cu, Al-Cu-Mg and Al-Cu-Mg-Si alloys[38–40] which, depending on the Cu and Mg content and ageing temperature,[12] may lead to a greatly increased strength relative to alloy A356. When the alloys are over aged, unlike the (MgSi) precipitates[41] that strengthen Al-Mg-Si alloys and which are easily cut by dislocations even when the alloy is overaged,[42,43] Cu-rich precipitates become increasingly resistant to cutting by dislocations, leading to increased strain hardening rates due to Orowan looping.[44,45]

Results

The analysis of the mechanical behaviour is based on material with SDAS 25 μm due to its higher ductility and low porosity content. Stress-strain flow curves of the alloys studied are presented in Figs 1 to 5. Plotted flow curves correspond to the most ductile specimen of each composition. The flow curve of alloy 21 (A356) has been included in all figures to serve as a common reference. It is important to bear in mind that the applied solution heat treatment of the present experiments is not standard for alloy A356. The point of failure of all specimens tested for selected alloys has been indicated on some of the flow curves as an example of the scatter observed in the tensile testing. Mean experimental values for all tested

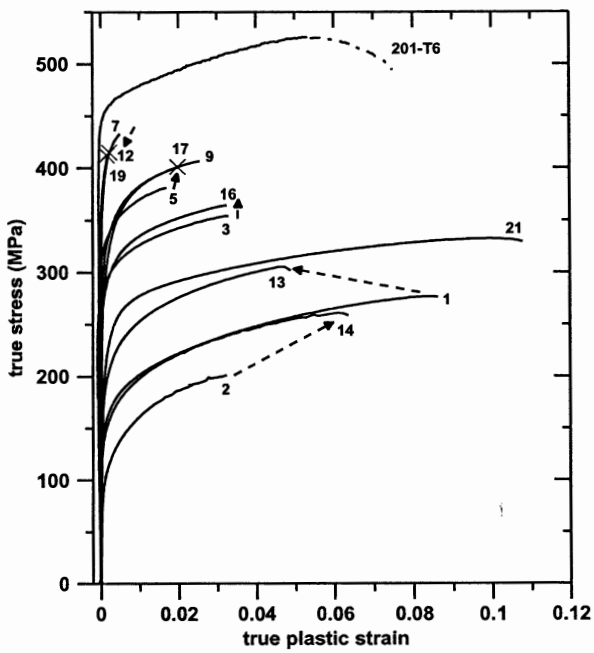

Fig. 1 True stress – true plastic strain curves of selected alloys showing that increased Si content generally increases the flow strength but may or may not increase the ductility. The arrows (1→13), (3→16) and (5→17) indicate the effect at low Mg and Cu; low Cu, high Mg; and high Cu, low Mg, respectively. Comparison of alloys 7, 12 and 19 shows decreasing ductility at high levels of Cu and Mg while the arrow (2→14) shows decreasing ductility at high Fe, low Cu and Mg content, with increased Si. A similar increase in ductility in alloys with high Fe can be seen in Fig. 4, alloys (4→15) and (6→18). The flow curve of alloy 201-T6 has been replotted from ref. 44 (see Discussion)

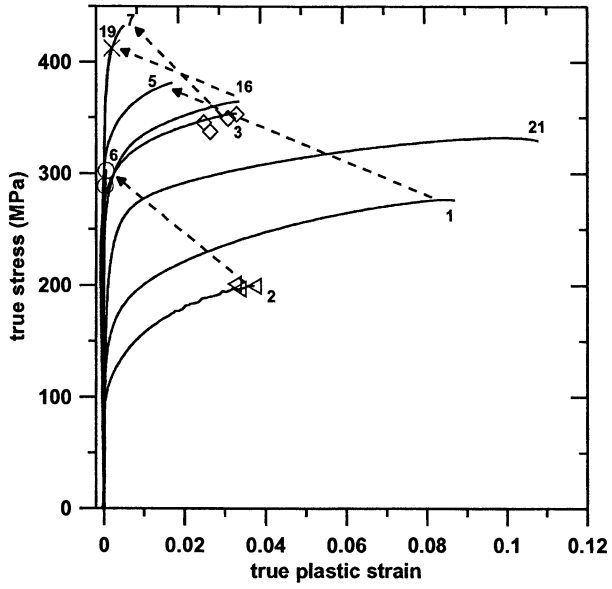

Fig. 2 True stress – true plastic strain curves of selected alloys showing that increased Cu systematically increases the strength and decreases the ductility. Arrows indicate the effect in alloys with low Si and low Mg and Fe (1→5); high Mg, low Fe (3→7); high Mg and Fe (2→6) and high Si and Mg, low Fe (16→19) alloys. A similar effect can be seen in Fig. 1, alloys (13→17) and in Fig. 4, alloys (14→18). The symbols indicate the point of failure of individual specimens in alloys 2, 6 and 16

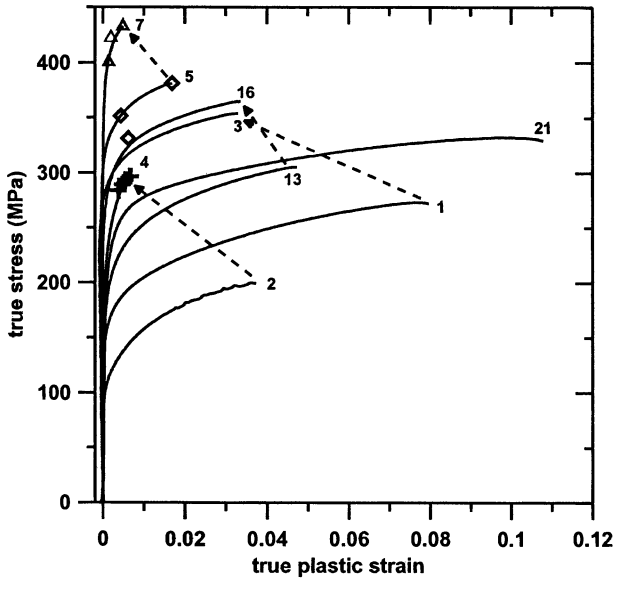

Fig. 3 True stress – true plastic strain curves of selected alloys showing that increased Mg systematically increases the strength and decreases the ductility. The arrows indicate the effect in alloys with low Si and Cu and low Fe (1→3) or high Fe (2→4); low Si and Fe and high Cu (5→7); and high Si, low Cu and Fe (13→16). The symbols indicate the point of failure of individual specimens in alloys 4, 5 and 7

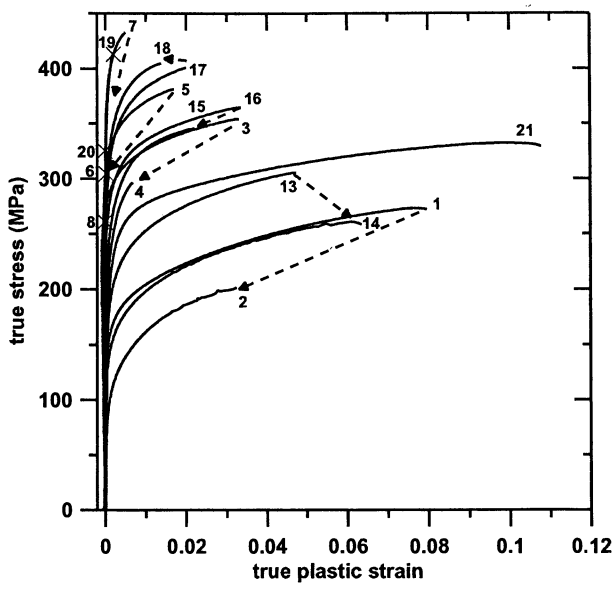

Fig. 4 True stress – true plastic strain curves of selected alloys showing the deleterious effects of increased Fe content on the flow behaviour. The arrows show the effect in low Si alloys with low Cu and Mg (1→2); low Cu, high Mg (3→4); low Mg, high Cu (5→6); high Cu and Mg (7→8); high Si alloys with low Cu and Mg (13→14); low Cu, high Mg (16→15); high Cu, low Mg (17→18) and high Cu and Mg (19→20)

specimens and calculated parameters have been condensed in Appendix A, Table A-3. The details of the analysis are in the captions to Figs 1 to 5, with only the main conclusions stated in the text. Not all of the alloys

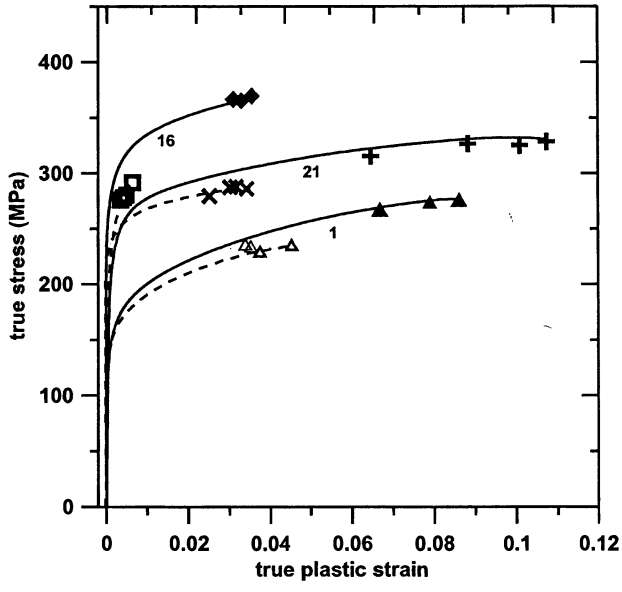

Fig. 5 True stress – true plastic strain curves of alloys 1, 16 and 21, showing that increasing the SDAS decreases the ductility. The solid and dashed flow curves correspond to specimens with SDAS 25 and 50 μm, respectively. The point of failure of all of the specimens tested has been indicated for each alloy

studied are included in Figs 1 to 5. A more comprehensive analysis is presented later in the text.

The flow curves of Fig. 1 show that increasing the (nominal) Si content from 4.5 to 7 or 9%, generally increases the flow stress, and tends to increase the ductility. Note the particularly high increase in ductility of the high Fe alloy 14 in comparison with alloy 2. There are two exceptions: the low Cu, Mg and Fe alloy 13 becomes less ductile than alloy 1, and the high strength alloys 7, 12 and 19 (i.e., with high contents of Mg and Cu), in which increasing Si from 4.5 to 7 to 9% progressively reduces the ductility and the tensile strength.

Fig. 2 shows that increased Cu generally results in a large increase in flow stress and decrease in ductility, at both low and high contents of Si.

The flow curves in Fig. 3 show that increased Mg increases the flow stress and decreases the ductility in all alloys, similarly to Cu in Fig. 2. The simultaneous increase of Mg and Cu magnifies the effects, as can be seen in Fig. 1 by comparing alloys (1 → 7) and (13 → 19).

In Fig. 4, increased Fe tends to lower both the ductility and the strength, although the effect is less clear in the alloys with high content of Si.

Fig. 5 shows the effect of changing the solidification rate, as measured by the SDAS, for alloys 1, 16 and 21. The yield strength and strain-hardening rate are only slightly affected, whilst the ductility experiences a dramatic decrease at large SDAS.

Discussion

Strength-ductility behaviour

The following analysis is based on a strength-ductility chart built following Appendix B. Power functions of the form of Eq. B1 were determined for each of the alloys. The K and n values for each alloy are given in Table A-3. The ductility of alloys 6, 8 and 20 was too low for a meaningful determination of K and n values. By comparison with more ductile alloys of comparable strength, a K-value of 560 MPa was assigned to them (asterisked values in Table A-3). The K-values range between about 400 and 560 MPa, so, for convenience, a mean value for $K = 490$ MPa was adopted to produce the chart of Fig. 6 using Eqs. B2 and B4. Note that the y-intersection of any given flow curve represents the (0.2%) proof stress of specimens whose data points lie on that line.

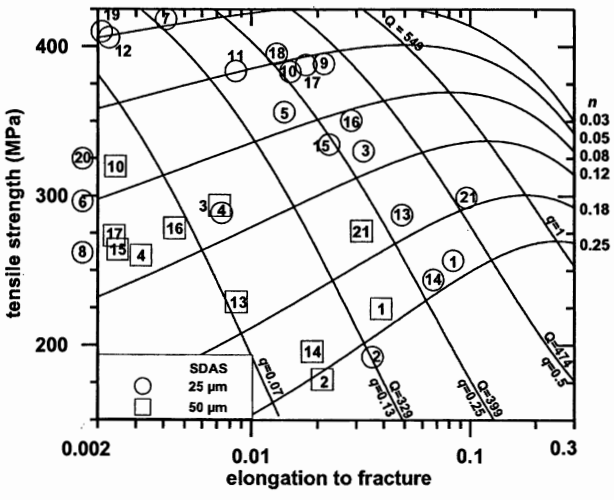

Fig. 6 A quality index chart for the alloys studied, obtained as described in Appendix B, with $K = 490$ MPa and given n-values. The circles and squares represent alloys with SDAS 25 μm (data from Table A3) and 50 μm, respectively. Alloys 6, 8 and 20 failed before the reaching the 0.2% proof stress. Of the alloys with SDAS 50 μm, only the most ductile have been plotted

The chart of Fig. 6 includes experimental points representing the mean values of the tensile strength and ductility observed for each of the alloys studied, for small and large SDAS. Within the material with SDAS 25 μm, alloy 21 stands out as the material with highest Q and q-values, while the bulk of the Cu-containing alloys lies around the line $q = 0.25$, $Q = 399$ MPa, with alloys 9, 10, 17 and 18 being the best performers in terms of proof stress, tensile strength and ductility. The points corresponding to SDAS 50 μm (squares) are located near the bottom left corner of the chart, due to their coarser microstructures and a higher porosity content. As the strength of the alloys is increased, the data points for both SDAS shift toward the upper left corner of the chart, with a continued decrease in Q and q-values. The tendency is more marked in the material with SDAS 50 μm. These trends closely agree with the predictions of Fig. C-2 of Appendix C, supporting the assumption that particle cracking is the main ductility-controlling factor in these materials.

A graphical depiction of the effect of the individual alloy components is presented in Fig. 7. In general terms, alloy additions that increase the strength, i.e., Cu and Mg, do so at the expense of ductility, and the overall effect is a loss in both Q and q-value. On the other hand, increased Fe or a larger SDAS shift the data points along single flow lines, causing a decrease in Q and q at constant proof stress. This is a common observation in quality index charts of alloy A356.[46]

A most interesting observation, pointed out with reference to alloys 2 and 14 in Fig. 1, is that of the increased ductility of the alloys with 9%Si content and high content of Fe, in comparison with the equivalent alloys at 4.5%Si. For example, increased Fe at low Si (1 → 2), lowers the strength and ductility, but increased Si at high Fe (2 → 14) restores most of the ductility. Similar sequences are presented by alloys (3 → 4 → 15) and (5 → 6 → 18). The flow curves of these alloys can be seen in Fig. 4. The increased ductility in high Fe alloys is indicated in Fig. 7 by dashed arrows.

This effect can be understood in terms of the relative tendency to form pre-eutectic α-$Al_{15}(Mn, Fe)_3Si_2$ particles and β-Al_5FeSi plates of alloys with different Si contents. Following Backerud[18] and others,[5,34] the process is illustrated in Fig. 8, where the Al-Si-Fe phase diagram is shown schematically for two alloys with

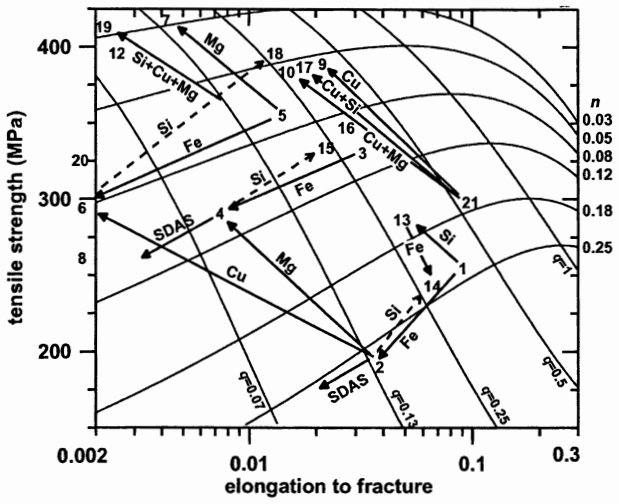

Fig. 7 The quality index chart of Fig. 6, with the effect of increasing the content of different elements or the SDAS indicated by arrows. For clarity, only alloys with SDAS 25 μm have been labelled. The dashed line arrows indicate the effect of increased Si on the low Si, high Fe-content alloys 2, 4 and 6

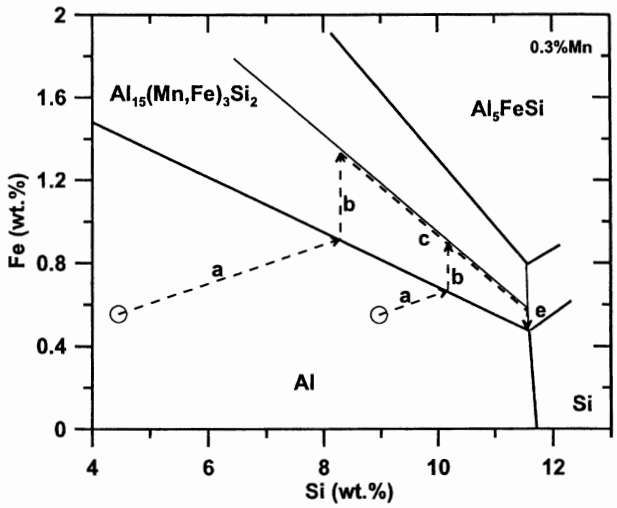

Fig. 8 A simplified Al-Si-Fe phase diagram (after Backerud *et al.*[18]) for alloys with 0.3%Mn. The dashed line arrows are the segregation lines (schematic) for two alloys with 0.5%Fe and 4.5 and 9%Si initial concentrations, respectively

0.3%Mn.* The dashed lines (a) indicate the increase in Fe and Si concentration as the dendritic structure develops in the primary α-Al field, calculated according to Scheil's equation, for a starting 0.5%Fe content and 4.5%Si and 9%Si. The vertical arrows (b) indicate schematically the formation of $Al_{15}(Mn,Fe)_3Si_2$, which occurs until the trough between the $Al_{15}(Mn,Fe)_3Si_2$ and Al_5FeSi phases is reached. The reaction continues involving both α and β along the dashed line (c) until the ternary eutectic composition (e) is reached, whereupon Al, Si and β-phase particles crystallise together. It is seen that for high Fe alloys with 4.5%Si (alloys 2, 4, 6 and 8) the period of formation of pre-eutectic Fe-rich intermetallics (and hence their size) is much larger than for the alloys with 9%Si (alloys 14, 15, 18 and 20). Pre-eutectic intermetallics also tend to be much larger than those that grow in the tight interdendritic channels during the ternary eutectic reaction and, therefore, are much more detrimental to the ductility. Metallographic evidence of the phases formed has been published elsewhere.[15]

In the same context, note that increased Si does not restore the ductility to alloy 20 in the sequence (7 → 8 → 20). There may be two concurrent effects in this case, one stemming from the level of Fe in alloy 20 being above target (0.7%, Tables A1 and A2). The other stems from the high strength of alloy 20 resulting from its high Cu and Mg contents. Strength effects on the ductility are considered later in the text.

It was noted in Fig. 1 that Si tends to increase the ductility of all of the alloys. In fact, although in a less dramatic fashion, the sequences noted above for the alloys with high Fe can be seen in Figs 6 and 7 for alloys with low Fe and low Cu and Mg, (1 → 13); low Cu, high Mg, (1 → 3 → 16); or low Mg, high Cu, (1 → 5 → 17). The effect seems to be stronger in the latter case, i.e., high Cu alloys. As for the high Fe alloys, the sequence breaks down when both Cu and Mg are increased simultaneously, i.e., (1 → 7 → 12 → 19). It is speculated that at high Si content the morphology or the balance of the phases forming are slightly altered in the sense of improving the ductility. This seems to be an area worthy of a closer look.

Upper bound to the strength

The model described at the end of Appendix C allows for a more comprehensive analysis of the data by means of the quality index-strength chart of Fig. 9. Using Eq. B2, the scale of the top x-axis in Fig. 9 has been expressed as the (0.2%) proof stress, Y, for $n = 0.1$, so the chart can be read in terms of Q, q and Y. Similarly to Fig. 6, the line labelled $q = 1$ indicates the onset of necking.

The solid lines of Fig. 9 indicate the expected trends in Q as the strength (as given by either K or Y) is increased, for three n-values. A maximum in Q is predicted for $K = 400$–500 MPa, depending on n. As explained in Appendix C, the solid lines of Fig. 9 indicate the expected trends when the ductility of the material is controlled by particle cracking.

Within the data points with SDAS 25 μm, alloy 21 is the only one that reaches the theoretical limit imposed by necking (line $q = 1$). The closest alloys (alloys 1, 3, 9 and 13 to 16) exhibit decreasing relative ductility, from $q \approx 0.5$ to $q \approx 0.25$, as the K-value increases. As for Fig. 6, for large SDAS (open squares) the mechanical performance worsens considerably.** The high Fe, low Si

* It should be noted that the formation of intermetallics during solidification is complex and the model of Fig. 8 is only one method of analysing the process. Modelling of the alloys using current solidification software packages indicates somewhat different outcomes. This is an area worthy of further study.

** Note that the charts of Figs 6 and 9 are not completely consistent (e.g., alloy 21 is above the line $q = 1$ in Fig. 9 but well below the same line in Fig. 6). This is because the chart of Fig. 6 was produced with a single K-value (490 MPa) while the position of the data points in Fig. 9 represent the actual K-value for each alloy as listed in Table A-3.

alloys 2, 4, 6 and 8 exhibit the lowest Q values, as expected from Figs 6 and 7. On the other hand, the tolerance to higher contents of Fe by the alloys with high Si is evident from the high Q-values of alloys 14, 15 and 18. Again, note the beneficial effect of increased Si in the low Fe alloys, especially when the Mg or Cu contents are increased, e.g., (1 → 13), (3 → 16) or (5 → 17). The Si content can thus be considered a very important alloy selection criterion for all alloys, not just for alloys with high contents of Fe.

The most significant feature of Fig. 9 is the abrupt fall of the Q values at $K \approx 560$ MPa (or in terms of the top x-axis, at Y ≈ 340 MPa). Note that the drop in Q-value is in close correspondence with the theoretical lines for $n = 0.05$ and $n = 0.1$. The fall in Q-value relates to the rapid loss of ductility of the stronger alloys, which in Fig. 9 is indicated by the decreasing q-values. In practical terms, Fig. 9 indicates the existence of an upper bound to the strength of these materials (at about 340 MPa) for the applied solution heat treatment. The existence of an upper bound to the strength relates to three factors which control the rate of particle cracking with the strain: (i) the strength of the alloy matrix; (ii) the increased tendency to form intermetallic particles as the Cu and Mg levels are increased (Table 1); (iii) particle clustering on the dendritic boundaries. Points (i) and (iii) are discussed in the next two sections.

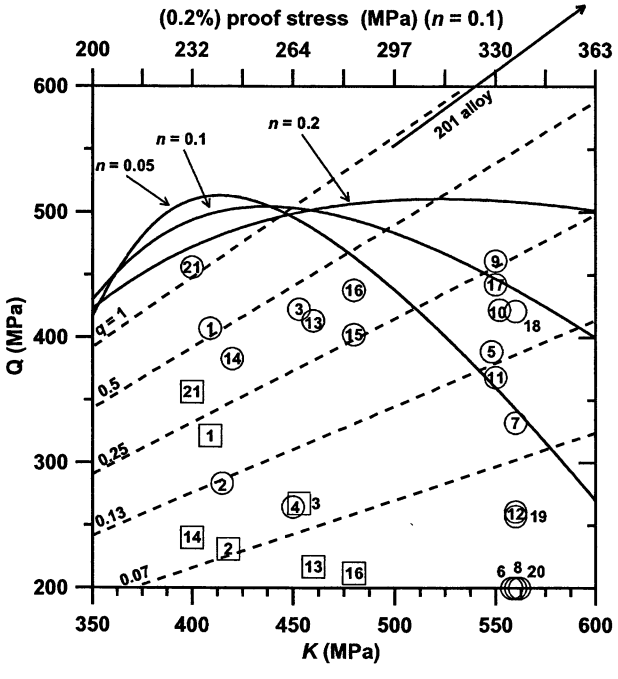

Fig. 9 The quality index, Q, as a function of the matrix strength coefficient, K, for given S* and n values. The solid lines represent the upper bound to the Q value imposed by particle cracking (see Appendix C). The dashed lines have been calculated with Eq. B8. The scale of the top x-axis has been calculated with Eq. B2. Circles and squares as in Fig. 6. The datum point representing 201-T6 alloy falls off scale at $K = 640$ MPa, Q = 710 MPa, on the line $q = 1$ (see §5.4)

Damage by particle cracking and tensile behaviour

The flow behaviour discussed in Figs 1 to 5 can be rationalised in simple terms considering the alloys as particulate metal matrix composites,[47–49] the eutectic Si and the Cu, Mg and Fe-rich intermetallic particles playing the role of the dispersed reinforcing phase. When particulate composites are plastically deformed, the reinforcing particles remain elastic while the matrix deforms plastically. This creates incompatibility stresses in both particles and matrix,[48–50] which lead to a very high strain-hardening rate at low strains. At strains of the order of 1–2%, plastic relaxation occurs near the tip of the reinforcing particles, decreasing the strain hardening rate to that of the unreinforced alloy, giving rise to a rounded flow curve. This type of rounded flow curve is absent in the unreinforced matrix[48] (i.e., without eutectic Si particles) and in the wrought[51] Al-Mg-Si alloys. When the flow curves of the alloy with reinforcing particles and that of the unreinforced alloys are plotted together, the flow stress of the reinforced alloy is higher by an amount proportional to the volume fraction of particles.[48,50,51]

The effect of increased volume fraction of reinforcement is illustrated by the increased flow strength of alloy 13 (9%Si) in comparison with alloy 1 (4.5%Si) in Fig. 1. Note that both alloy 1 and 13 have low contents of Mg, Cu and Fe, and the intermetallic phases that form do not change with the increased Si, so the observed effects can be ascribed to the difference in Si content.

The increased strength and decreased ductility of alloys with high Cu and/or Mg described in Figs 2 and 3 can be understood as follows. The shedding of load onto the dispersed particles is enhanced and particle cracking occurs at lower strains, lowering the ductility, when the alloy matrix is strengthened by precipitation, which delays the onset of plastic relaxation.[48,52,53] The ductility is also decreased when the reinforcing particles are large or elongated.[54] Alloys with high content of both Cu and Mg represent a worst-case scenario since both solutes enhance the precipitation strengthening of the alloy matrix as well as increase the content of intermetallics (Table 1).

Table 1 suggests that the decreased ductility of the alloys with high content of Fe discussed in Fig. 4 can be ascribed to the formation of brittle α-$Al_{15}(Fe,Mn)_3Si_2$ particles in conjunction with β-phase platelets as well as π-phase particles in the high Mg alloys. Any dispersion hardening effects due to the increased volume fraction of Fe-rich intermetallics is likely to be more than offset by the depletion of Mg from the alloy matrix, as discussed in the introduction, which explains the lower flow stress of alloys with high content of Fe. The same concepts rationalise the effect of large SDAS in Fig. 5, since low solidification rates result in the formation of large Fe- and Cu-rich intermetallic particles.[7] Large particles are difficult to break up during the solution heat treatment and lower the ductility.[9] The effect of solidification rate is compounded by the tendency of the alloys to develop higher levels of porosity at low solidification rates.[2,3,7,14]

Role of particle clustering

The dendritic structure introduces an additional element in the fracture process of these alloys, which is paramount in determining the upper bound to the strength discussed in relation to Fig. 9. The micrograph of Fig. 10 shows that dendritic boundaries can be considered clusters of second phase particles that divide the deforming material in the same way grain boundaries do.[49,55,56] Particle clusters in a deforming composite present a highly constrained state in which the matrix is locally shielded from plastic deformation.[57] Stresses inside the clusters increase rapidly with the strain due to the lack of local plastic relaxation,[57,58] until the largest intermetallic particles crack, progressively shedding load onto the remaining particles. This creates microcracks along the dendritic boundaries, which lead to macroscopic fracture.[55] As the strength of the alloy matrix is increased by precipitation hardening, the fracture process becomes increasingly critical and occurs at increasingly lower strains. In the limit, fracture occurs right after yield, which is what Fig. 9 shows at $K \approx 560$ MPa.

The damage sequence can be pictured as follows: the large β-Al_5FeSi plates in low Si, high Fe alloys crack first, followed by the rest of the intermetallics. The small and round Sr-modified Si particles are the last ones to crack, leading to macroscopic fracture. At low contents of Cu and Mg the constraint in the clusters is limited, and the cracking of eutectic Si occurs over a strain of several %. Conversely, at high contents of Cu and Mg, the constraint in the clusters is at its peak and the cracking of the large intermetallics is followed right away by the cracking of the eutectic Si. Indeed, the fracture of the alloys with high Cu and Mg content is a very localised event which involves little particle cracking aside from those particles at or very near the fracture surface (see for instance the metallographic study by Gauthier *et al.*[12]). This behaviour is in contrast with the more ductile alloy A356, in which damage by particle cracking may accumulate over 10–12% in strain and spreads over the entire gauge length.[52,59–62]

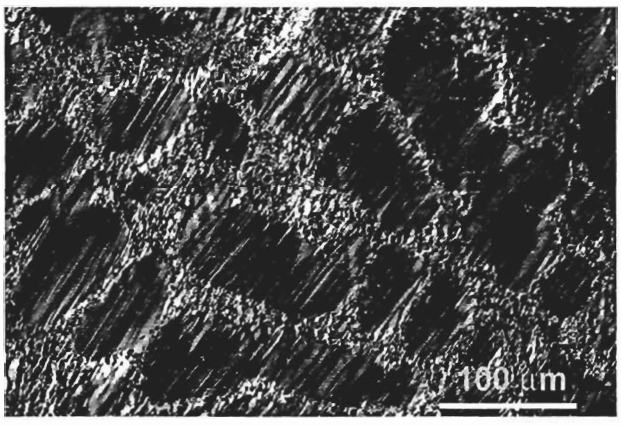

Fig. 10 Example of the interaction between dendritic cells and plastic deformation in a Sr-modified A356-T6 alloy. Photomicrograph taken under Nomarski interference contrast on the surface of a specimen polished prior to tensile straining. SDAS 50 μm, applied strain 3%. The tensile axis is horizontal

It is of interest at this point to explore the conditions that would allow a high strength alloy to reach higher Q values, i.e., above the limits imposed by the solid lines of Fig. 9. From the discussion above, catastrophic cracking of eutectic Si in the interdendritic clusters imposes the upper limit to the strength of the alloys. Therefore, elimination of the eutectic Si should dramatically improve the strongest alloys' Q-values. This point can be easily proved by comparing the alloys of this study with the (Si-free) high-strength casting alloy 201 (Al-4Cu-Mg-Ag), whose flow curve[44] has been included in Fig. 1. It is seen that this alloy deforms up to necking at very high stress levels (> 500 MPa). For 201 alloy in T6 temper,[44] $K = 640$ MPa, $Q = 710$ MPa and $q = 1$, which locate this alloy well above any of the (Si containing) alloys of this study (see arrow in Fig. 9).

Alloy selection

For a given Fe content, the intensity of precipitation hardening and the type and amount of intermetallic particles are controlled by the combined contents of Cu and Mg. On the other hand, deleterious effects on the ductility caused by a high Fe content can be neutralised with a high content of Si, which also tends to increase the ductility in alloys with high contents of Mg or Cu. Thus, it seems that an alloy selection criterion should involve only Cu, Mg and Si.

If the alloys are sorted in terms of the (Cu + Mg) content in at.% (see values in Table A-1), with reference to the data for SDAS 25 μm in Fig. 9, alloys with (Cu + Mg) < 1.6 at.% are to the left or at the center of the chart, while alloys on the vertical line at $K \approx 560$ MPa have (Cu + Mg) > 1.65 at.%, in monotonic correspondence with decreasing Q and q values. The high Si alloys 9, 10, 17 and 18, with (Cu + Mg) 1.65 1.95 at.%, combine the highest Q, q and Y values and thus offer the best compromise in terms of proof stress (330 340 MPa), tensile strength (380–395MPa) and ductility (1.5–2%). Lower (Cu + Mg) values (< 1.6 at.%) lead to lower Y-values at constant Q, while higher (Cu + Mg) values (> 2 at.%) lead to a rapid drop in Q and q. In practical terms, for optimal mechanical performance (as given by Q, q and Y) the alloys should have a high content of Si (7.5 to 9%) to maintain the ductility at high levels of Fe (at Mn:Fe ratio 0.5), and the Cu content should be limited to 3% when the Mg level is above 0.1%. Conversely, alloys with 4% Cu can only contain 0.1% Mg.

Summary and conclusions

A comparison of 20 experimental Al-Si-Cu-Mg alloys has been carried out to assess the effect of varying contents of Si, Cu, Mg and Fe (at Fe/Mn ratio 0.5 for the higher Fe content), as well as the solidification rate, on the mechanical properties, in T6 temper.

The strength of the alloys increases with increasing content of Mg and/or Cu. In all cases the ductility

decreases as well. A higher content of Fe generally reduces the strength and ductility.

Strength-ductility and quality index-strength charts have been developed for the alloys. These charts allow for a systematic analysis of the effect of different alloy components or solidification rate on the mechanical behaviour.

The strength-ductility chart shows that increased Si systematically increases the strength and the ductility of most alloys, especially when the Fe content is high. The latter is due to the reduced tendency of high Si content alloys to form large pre-eutectic α-$Al_{15}(Mn,Fe)_3Si_2$ particles and β-Al_5FeSi plates during solidification.

The quality index-strength chart has been used to show that the cracking of second phase particles at low strains imposes a limit on the maximum achievable strength by severely reducing the ductility of alloys with high contents of Cu and Mg. The maximum proof stress of alloys exhibiting about 1.5–2% tensile ductility is approximately 340 MPa.

The alloys can be sorted in terms of strength and ductility by the combined (at.%) content of Cu and Mg and the Si content. High Si content alloys are likely to exhibit ductility in excess of 1.5–2% if the (Cu + Mg) content is less than 1.95 at.%. This implies a maximum Cu content of 3% for alloys with Mg contents above 0.1%. Alloys with (Cu + Mg) contents > 2 at.% are likely to fail at yield, especially at low Si and high Fe contents.

Acknowledgement

The authors are indebted to D. A. Graham for help with the mechanical testing and to C. J. Davidson for critical comments on the manuscript. CAST was established and is funded in part by the Australian Government's Cooperative Research Centres Program.

References

1. A. M. Samuel and F. H. Samuel, "A metallographic study of porosity and fracture behaviour in relation to the tensile properties in 319.2 end chill castings", *Metall. Mater. Trans.*, 1995, **26A**, 2359–2372.
2. N. Roy, A. M. Samuel and F. H. Samuel, "Porosity formation in Al-9wt%Si-3wt%Cu alloy systems: metallographic observations", *Metall. Mater. Trans.*, 1996, **27A**, 415–429.
3. G. A. Edwards, G. K. Sigworth, C. H. Cáceres, D. St John and J. Barresi, "Microporosity formation in Al-Si-Cu-Mg casting alloys", *AFS Trans.*, 1997, **105**, 809–818.
4. R. DasGupta, C. C. Brown and S. Marek, "Effect of increased magnesium content on the mechanical properties of sand-cast 319 aluminum alloy", *AFS Trans.*, 1989, **97**, 245–254.
5. L. Anantha Narayanan, F. H. Samuel and J. E. Gruzleski, "Crystallization behaviour of iron-containing intermetallic compunds in 319 aluminum alloy", *Metall. Mater. Trans.*, 1994, **25A**, 1761–1773.
6. L. Wang and S. Shivkumar, "Strontium modification of aluminium alloy castings in the expendable casting pattern process", *J. Mater. Sci.*, 1995, **30**, 1584–1594.
7. F. H. Samuel, A. M. Samuel and H. W. Doty, "Factors controlling the type and morphology of copper-containing phases in 319 aluminum alloy", *AFS Trans.*, 1996, **104**, 893–901.
8. J. Gauthier, P. R. Louchez and F. H. Samuel, "Heat treatment of 319.2 aluminium automotive alloy. Part 1, Solution heat treatment", *Cast Metals*, 1995, **8**, 91–106.
9. H. de la Sablonière and F. H. Samuel, "Solution heat treatment of 319 aluminium alloy containing 0.5% Mg. Part I-solidification and tensile properties", *Int. J. Cast Metals Res.*, 1996, **9**, 195–211.
10. H. de la Sablonière and F. H. Samuel, "Solution heat treatment of 319 aluminium alloy containing 0.5% Mg. Part II-microstructure and fractography", *Int. J. Cast Metals Res.*, 1996, **9**, 213–225.
11. P. Ouellet, F. H. Samuel, D. Gloria and S. Valtierra, "Effect of Mg content on the dimensional stability and tensile properties of heat treated Al-Si-Cu (319) type alloys", *Int. J. Cast Metals Res.*, 1997, **10**, 67–78.
12. J. Gauthier, P. R. Louchez and F. H. Samuel, "Heat treatment of 319.2 aluminium automotive alloy. Part 2, Ageing behaviour", *Cast Metals*, 1995, **8**, 107–114.
13. C. H. Cáceres, J. H. Sokolowski and P. Gallo, "Effect of ageing and Mg content on the Quality Index of two Al-1%Cu–4.5%Si-Mg alloys", *Mater. Sci. Engng. A*, 1999, **271**, 53–61.
14. G. K. Sigworth and C. H. Cáceres, "Porosity formation in aluminium alloy castings under quasi-directional solidification", *Int. J. Cast Metals Res.*, 1997, **9**, 331–336.
15. R. Smith, C. H. Cáceres and D. St John, "The microstructure of Al-Si-Cu-Mg alloys", *Materials Research 96*, Brisbane, Australia, The Institute of Metals and Materials Australasia, 1996, pp. 140–143.
16. Comalco Aluminium Ltd., *Casting of metal objects*, US, Patent No 5297611, 1996.
17. L. F. Mondolfo, *Aluminium alloys: structure and properties*, Butterworths, London, 1976, p. 971.
18. S. L. Backerud, G. Chai and J. Tamminen, *Solidification characteristics of aluminium alloys*, AFS/Skanaluminium, Oslo, Norway, 1990.
19. I. J. Polmear, *Light Alloys*, Edward Arnold, London, 1995.
20. M. H. Mulazimoglu, N. Tenekedjiev, B. Closset and J. Gruzleski, "Studies on the minor reactions and phases in strontium-treated aluminium-silicon casting alloys", *Cast Metals*, 1993, **6**, 16–28.
21. M. B. Djurdjevic, T. J. Stockwell and J. H. Sokolowski, "The effect of strontium on the microstructure of the aluminum-silicon and aluminum – copper eutectics in the 319 aluminum alloy", *Int. J. Cast Metals Res.*, 1999, **12**, 67–73.
22. S. D. McDonald and J. A. Taylor, (*in preparation*), 2002.
23. N. Tenekedjiev, H. Mulazimoglu, B. Closset and J. Gruzleski, *Microstructures and thermal analysis of strontium-treated aluminium-silicon alloys*, American Foundrymen's Society, Des Plaines, 1995, p. 81.
24. C. H. Cáceres, M. B. Djurdjevic, T. J. Stockwell and J. H. Sokolowski, "The effect of Cu content on the formation of microporosity in Al-Si-Cu-Mg alloys", *Scripta Mater.*, 1998, **40**, 631–637.
25. P. A. Rometsch, L. Arnberg and D. L. Zhang, "Modelling dissolution of Mg_2Si and homogenisation in Al-Si-Mg casting alloys", *Int. J. Cast Metals Res.*, 1999, **12**, 1–8.
26. G. A. Edwards, K. Stiller, G. L. Dunlop and M. J. Couper, "The composition of fine-scale precipitates in Al-Mg-Si alloys", *Mater. Sci. Forum*, 1996, **217–222**, 713–718.

27. G. E. Nagel, J. P. Mouret and J. Dubruelh, ''A 357 type alloy with improved properties'', *AFS Trans.*, 1983, **91**, 157–160.
28. D. A. Granger, R. R. Sawtell and M. M. Kersker, ''Effect of beryllium on the properties of A357.0 castings'', *AFS Trans.*, 1984, **92**, 579–586.
29. J. A. Taylor, D. H. St John, J. Barresi and M. J. Couper, ''Influence of Mg content on the microstructure and solid solution chemistry of Al-7%Si-Mg casting alloys during solution treatment'', *Materials Science Forum*, 2000, **331–337**, 277–282.
30. C. H. Cáceres, C. J. Davidson, J. R. Griffiths and Q. G. Wang, ''The effect of Mg on the microstructure and mechanical behaviour of Al-Si-Mg casting alloys'', *Metall. Mater. Trans.*, 1999, **30A**, 2611–2618.
31. A. Couture, ''Iron in aluminum casting alloys: a literature survey'', *AFS Int. Cast Metals Jnl.*, 1981, **6**, 9–17.
32. P. N. Crepeau, ''Effect of iron in Al-Si alloys: a critical review'', *AFS Trans.*, 1996, **103**, 361–366.
33. J. A. Taylor, G. B. Schaffer and D. St John, ''The role of iron in porosity formation in Al-Si-Cu based casting alloys – Part I: Initial experimental observations'', *Metall. Mater. Trans.*, 1999, **30A**, 1643–1650.
34. J. A. Taylor, G. B. Schaffer and D. St John, ''The role of iron in porosity formation in Al-Si-Cu based casting alloys – Part II: A phase diagram approach'', *Metall. Mater. Trans.*, 1999, **30A**, 1651–1655.
35. J. A. Taylor, G. B. Schaffer and D. St John, ''The role of iron in porosity formation in Al-Si-Cu based casting alloys – Part III: A microstructural model'', *Metall. Mater. Trans.*, 1999, **30A**, 1657–1662.
36. H. Iwahori, H. Takamiya, K. Yonekura, Y. Yamamoto and M. Nakamura, ''Influence of iron and manganese on feedability of AC2B aluminum alloy'', *Imono (Casting)*, 1988, **60**, 590–595.
37. M. C. Flemings, T. Z. Kattamis and B. P. Bardes, ''Dendrite arm spacing in aluminium alloys'', *AFS Trans.*, 1991, **99**, 501–506.
38. K. Hono, N. Sano, S. S. Babu, R. Okano and T. Sakurai, ''Atom probe study of the precipitation process in Al-Cu-Mg-Ag alloys'', *Acta Metall. Mater.*, 1993, **41**, 829–838.
39. I. J. Polmear, ''Control of precipitation processes and properties in aged aluminium alloys by trace elements additions'', Proc. of the 6th Intern. Conf. on Aluminium Alloys, ICAA-6, Toyohasi, Japan, Eds T. Sato, S. Kumai, T. Kobayashi and Y. Murakami, 1998, pp. 75–85.
40. W. Reif, J. Dutkiewicz, R. Ciach, S. Yu and J. Krol, ''Effect of ageing on the evolution of precipitates in AlSiCuMg alloys'', *Mater. Sci. Engng. A*, 1997, **A224–236**, 165–168.
41. G. A. Edwards, K. Stiller, G. L. Dunlop and M. J. Couper, ''The precipitation sequence in Al-Mg-Si alloys'', *Acta Mater.*, 1998, **46**, 3893–3904.
42. J. W. Martin, *Micromechanisms in particle hardened alloys*, Cambridge University Press, Cambridge, 1980, p. 122.
43. J. M. Dowling and J. W. Martin, ''The influence of Mn additions on the deformation behaviour of an Al-Mg-Si alloy'', *Acta Metall.*, 1976, **24**, 1147–1153.
44. C. H. Cáceres, T. Din, A. K. M. B. Rashid and J. Campbell, ''Effect of ageing on the Quality Index of an Al-Cu alloy'', *Mater. Sci. Technol.*, 1999, **15**, 711–716.
45. R. E. Stoltz and R. M. Pelloux, ''The Bauschinger effect in precipitation strengthened aluminium alloys'', *Metall. Trans.*, 1976, **7A**, 1295–1306.
46. M. Drouzy, S. Jacob and M. Richard, ''Interpretation of tensile results by means of quality index and probable yield strength'', *AFS Int. Cast Metals Jnl.*, 1980, **5**, 43–50.
47. W. H. Hunt, J. R. Brockenbrough and P. E. Magnusen, ''An Al-Si-Mg composite model system: microstructural effects on deformation and damage evolution'', *Scripta Metall. Mater.*, 1991, **25**, 15–20.
48. M. T. Kiser, F. W. Zok and D. S. Wilkinson, ''Plastic flow and fracture of a particulate metal matrix composite'', *Acta Mater.*, 1996, **44**, 3465–3476.
49. C. H. Cáceres, J. R. Griffiths and P. Reiner, ''The influence of microstructure on the Bauschinger effect in an Al-Si-Mg casting alloy'', *Acta Mater.*, 1996, **44**, 15–23.
50. L. M. Brown and W. M. Stobbs, ''The work hardening of copper-silica II. The role of plastic relaxation'', *Phil. Mag.*, 1971, **23**, 1201–1233.
51. Q. G. Wang and C. H. Cáceres, ''On the strain hardening behaviour of Al-Si-Mg casting alloys'', *Mater. Sci. Engng. A*, 1997, **A234–236**, 106–109.
52. J.-W. Yeh and W.-P. Liu, ''The cracking mechanism of silicon particles in an A357 aluminum alloy'', *Metallurgical and Materials Transactions*, 1996, **27A**, 3558–3568.
53. M. Manoharan, J. J. Lewandowski and W. H. J. Hunt, ''Fracture characteristics of an Al-Si-Mg model composite system'', *Mater. Sci. Engng. A*, 1993, **A172**, 63–69.
54. C. H. Cáceres and J. R. Griffiths, ''Damage by the cracking of silicon particles in an Al-7Si-0.4Mg casting alloy'', *Acta Mater.*, 1996, **44**, 25–33.
55. C. H. Cáceres, ''Particle cracking and the tensile ductility of a model Al-Si-Mg composite system'', *Alum. Trans.*, 1999, **1**, 1–13.
56. Q. G. Wang and C. H. Cáceres, ''The fracture mode in Al-Si-Mg casting alloys'', *Mater. Sci. Engng. A*, 1998, **A241**, 72–82.
57. D. S. Wilkinson, E. Maire and J. D. Embury, ''The role of heterogeneity on the flow and fracture of two-phase materials'', *Mater. Sci. Engng. A*, 1997, **A233**, 145–154.
58. D. J. Lloyd, ''Aspects of fracture in particulate reinforced metal matrix composites'', *Acta Metall. Mater.*, 1991, **39**, 59–71.
59. S. F. Frederick and W. A. Bailey, ''The relation of ductility to dendrite cell size in a cast Al-Si-Mg alloy'', *Trans. Metall. Soc. AIME*, 1968, **242**, 2063–2067.
60. R. C. Voigt and D. R. Bye, ''Microstructural aspects of fracture in A356'', *AFS Trans.*, 1991, **99**, 33–49.
61. C. H. Cáceres, C. J. Davidson and J. R. Griffiths, ''The deformation and fracture behaviour of an Al-Si-Mg casting alloy'', *Mater. Sci. Engng. A*, 1995, **A197**, 171–179.
62. Q. G. Wang, C. H. Cáceres and J. R. Griffiths, ''The cracking of Fe-rich and eutectic Si particles in an Al-7Si-0.7Mg casting alloy'', *AFS Trans.*, 1998, **106**, 131–136.
63. C. H. Cáceres, ''A rationale for the Quality Index of Al-Si-Mg casting alloys'', *Int. J. Cast Metals Res.*, 1998, **10**, 293–299.
64. C. H. Cáceres, ''A phenomenological approach to the Quality Index'', *Int. J. Cast Metals Res.*, 2000, **12**, 367–375.
65. G. E. Dieter, *Mechanical Metallurgy*, McGraw-Hill, New York, 1986, p. 290.
66. I. Justice, P. Poza, J. L. Martinez and J. Llorca, ''Reinforcement stresses during deformation of sphere- and particulate-reinforced Al-matrix composites'', *Metall. Mater. Trans.*, 1996, **27A**, 486–489.
67. Y. Brechet, J. D. Embury, S. Tao and L. Luo, ''Damage initiation in metal matrix composites'', *Acta Metall. Mater.*, 1991, **39**, 1781–1786.

Appendix A

Table A-1 Measured chemical composition of the alloys (wt.%)

Alloy	Si	Cu	Mg	Fe	Mn	Sr	Mn/Fe	Cu + Mg (at.%)
1	4.57	1.02	0.10	0.20	0.01	0.020	0.05	0.55
2	4.47	0.99	0.09	0.52	0.24	0.007	0.46	0.52
3	4.64	1.17	0.47	0.21	0.01	0.018	0.05	1.02
4	4.47	1.02	0.48	0.54	0.36	0.018	0.67	0.97
5	4.47	4.09	0.09	0.21	0.00	0.013	0.00	1.88
6	4.64	4.20	0.13	0.53	0.12*	0.019	0.23	1.97
7	4.68	3.99	0.48	0.21	0.00	0.018	0.00	2.27
8	4.80	4.40	0.52	0.56	0.28	0.012	0.50	2.49
9	7.39	3.03	0.31	0.17	0.00	0.049	0.00	1.65
10	7.90	3.12	0.53	0.20	0.01	0.023	0.05	1.94
11	7.91	4.08	0.33	0.19	0.01	0.024	0.05	2.14
12	7.66	4.34	0.54	0.19	0.00	0.040	0.00	2.49
13	8.48	1.11	0.15	0.18	0.00	0.024	0.00	0.64
14	8.50	0.96	0.09	0.48	0.46*	0.018	0.96	0.51
15	9.34	1.10	0.50	0.27*	0.01*	0.020	0.04	1.02
16	8.47	1.11	0.56	0.18	0.00	0.024	0.00	1.1
17	8.56	3.92	0.10	0.18	0.00	0.028	0.00	1.81
18	8.81	4.16	0.10	0.52	0.29	0.011	0.56	1.92
19	8.30	4.19	0.45	0.28	0.05	0.017	0.18	2.32
20	9.02	4.05	0.52	0.70*	0.30	0.016	0.43	2.34
21	6.68	0.00	0.28	0.14	0.00	0.017	0.00	0.31

Note: starred values indicate significant departure from targeted compositions, see Table A-2

Table A-2 Targeted chemical composition of the alloys (wt.%)

Alloy	Si	Cu	Mg	Fe	Mn	Sr	Mn/Fe
1	4.5	1.0	0.1	0.2	0	0.02	0
2	4.5	1.0	0.1	0.5	0.25	0.02	0.5
3	4.5	1.0	0.5	0.2	0	0.02	0
4	4.5	1.0	0.5	0.5	0.25	0.02	0.5
5	4.5	4.0	0.1	0.2	0	0.02	0
6	4.5	4.0	0.1	0.5	0.25	0.02	0.5
7	4.5	4.0	0.5	0.2	0	0.02	0
8	4.5	4.0	0.5	0.5	0.25	0.02	0.5
9	7.5	3.0	0.3	0.2	0	0.02	0
10	7.5	3.0	0.5	0.2	0	0.02	0
11	7.5	4.0	0.3	0.2	0	0.02	0
12	7.5	4.0	0.5	0.2	0	0.02	0
13	9.0	1.0	0.1	0.2	0	0.02	0
14	9.0	1.0	0.1	0.5	0.25	0.02	0.5
15	9.0	1.0	0.5	0.5	0.25	0.02	0.5
16	9.0	1.0	0.5	0.2	0	0.02	0
17	9.0	4.0	0.1	0.2	0	0.02	0
18	9.0	4.0	0.1	0.5	0.25	0.02	0.5
19	9.0	4.0	0.5	0.2	0	0.02	0
20	9.0	4.0	0.5	0.5	0.25	0.02	0.5
21	7.0	0.0	0.3	0.15	0	0.02	0

Table A-3 The (average values) tensile strength, TS, the (0.2%) proof stress, Y, and the plastic strain to fracture, s_f, of the alloys studied (SDAS 25 μm). The parameters K and n as defined in Eq. B1. The quality index Q was calculated with Eq. B7

Alloy number	TS (MPa)	Y (MPa)	s_f (%)	K (MPa)	n	Q (MPa)
1	256.7	169.9	8.32	409	0.16	407
2	192.2	118.9	3.55	415	0.21	284
3	330.2	266.7	3.24	453	0.07	422
4	288.7	250.8	0.74	450	0.08	264
5	356.2	323.0	1.41	548	0.1	388
6	296.3	–	0.07	560*	–	200*
7	418.4	405.7	0.41	560	0.05	331
8	261.9	–	0.03	560*	–	200*
9	388.7	324.0	2.14	550	0.08	461
10	383.3	336.0	1.50	552	0.08	422
11	383.8	340.3	0.85	550	0.08	368
12	406.0	403.9	0.23	560	0.05	260
13	287.4	208.5	4.85	460	0.13	413
14	243.9	156.8	6.75	420	0.17	376
15	334.7	275.6	2.26	480	0.09	402
16	350.6	279.3	2.85	480	0.08	437
17	387.9	337.6	1.77	550	0.08	442
18	395.4	346.5	1.30	560	0.08	421
19	410.0	410.0	0.21	560	0.05	257
20	325.0	–	0.04	560*	–	200*
21	298.8	242.1	9.60	400	0.08	456*

The ductility of alloys 6, 8 and 20 was too low for a meaningful determination of K, n and Q, so the values for K (560 MPa) and Q (200 MPa) were used

Appendix B. Analytical strength-ductility charts

Strength-ductility charts for casting alloys, first developed by Drouzy *et al.*,[46] are an efficient tool to compare on a common base the performance of different alloys or to assess the effect of changes to the alloy processing or chemical composition. Charts for any given material can be created using a simple continuum mechanics model.[63,64]

Let the deformation curves of the material be described with a power law relationship:

$$\sigma = K\varepsilon^{n}, \tag{B1}$$

where σ is the true flow stress, K is the alloy's strength coefficient, ε is the true plastic strain and n the strain hardening exponent.

The engineering stress-strain curve can be approximated by

$$P \cong K s^{n} e^{-s}, \tag{B2}$$

where P and s are the engineering values of the stress and the plastic strain, respectively. The flow lines in Fig. 6 (identified by the n-value) have been generated with Eq. B2.

The Considère criterion[65] applied to Eq. B1 indicates that necking starts at a tensile strain $\varepsilon = n$. It is convenient to define the relative ductility parameter, q:

$$q = \frac{s_f}{n}. \tag{B3}$$

where s_f is the elongation to fracture. For any specimen deforming up to necking, $q = 1$. By combining Eq. B3 and Eq. B2 the following equation for the iso-q contour lines in Fig. 6 (identified by the q-value) is obtained:

$$P = K s^{s_f/q} e^{-s_f}. \tag{B4}$$

Drouzy *et al.*[46] used their strength – ductility charts to define a "quality index" parameter, Q, as:

$$Q = TS + d\log(100 s_f), \tag{B5}$$

where TS is the tensile strength. The empirical constant d can be expressed as[64]

$$d = 0.4K. \tag{B6}$$

Combining with Eq. B5 :

$$Q = TS + 0.4K\log(100 s_f). \tag{B7}$$

Combining Eqs. B2, B3 and B7, Q can be approximated by[64]

$$Q \approx [1.12 + 0.22\ln(q)]K. \tag{B8}$$

Appendix C. Particle cracking and quality index

The effects of changing microstructural parameters (i.e., SDAS; size, shape and content of eutectic Si and Fe-rich intermetallic particles) on the quality index can be incorporated into the model of Appendix B using a simple particulate metal matrix composite approach.[64]

Finite element analysis has shown[66] that when the flow curve of the alloy matrix can be represented by an equation of the form of Eq. B1, the tensile stress, σ_p, developed in the reinforcing particles can be described with a similar equation,

$$\sigma_p = K_p \varepsilon^{n_p}, \tag{C1}$$

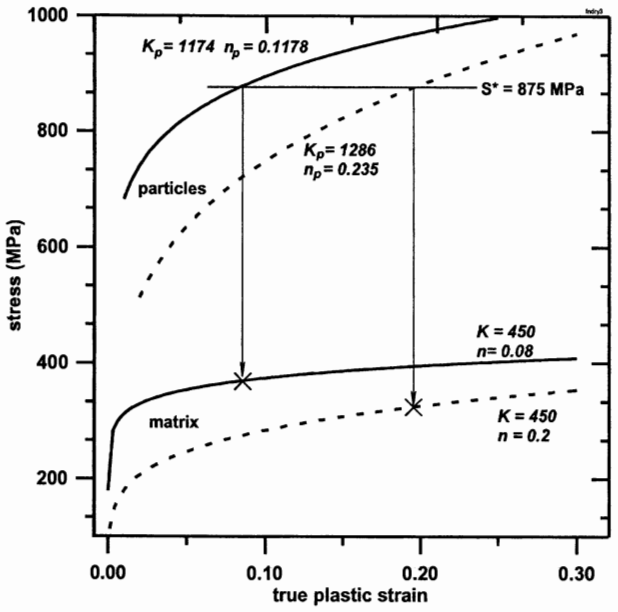

Fig. C-1 Flow curves for the matrix and corresponding particle stresses as functions of the applied strain, calculated with Eqs. B1 and C1, respectively. K, K_p, n and n_p as labelled. Fracture (indicated by the crosses) occurs when the particle stresses approach S* (= 875 MPa)[64]

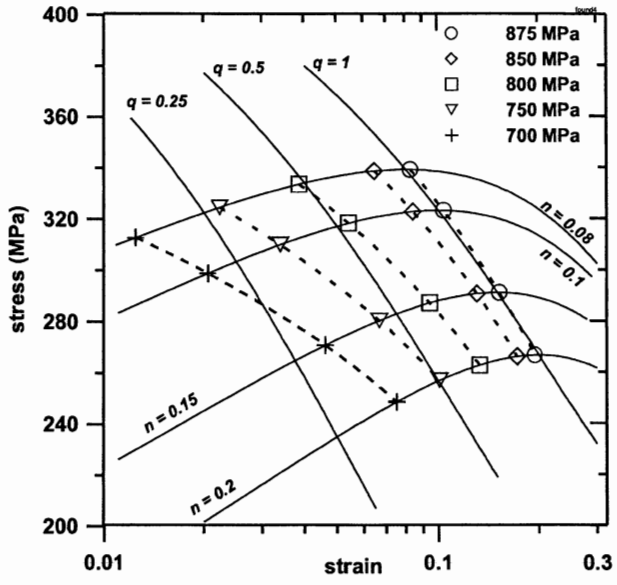

Fig. C-2 A comparison between the predictions of the continuum mechanics model (solid lines: Eqs. B3 and B5) and the model incorporating damage by particle cracking (symbols) for a material with $K = 450$ MPa, for different S*-values (see text)

where K_p and n_p are polynomial functions of the volume fraction of reinforcement, f, and the alloy matrix parameters K and n.

Equation C1 can be used to calculate the macroscopic fracture strength and strain of the alloys assuming that fracture occurs at a critical value of the applied plastic strain, ε_f, such that

$$\sigma_p^* = K_p \varepsilon_f^{n_p} \approx K_p s_f^{n_p} = S^* \qquad (C2)$$

where S* is the fracture stress of the reinforcing particles.

For a given S*, Eq. C2 can be solved for the elongation to fracture, s_f, and this value used in Eq. B2 to calculate the tensile strength of the material. The procedure is schematically shown in Fig. C-1, where the flow curves of a hypothetical material with matrix properties given by $K = 450$ MPa and given n-values, are plotted together with the corresponding particle stresses. When the stress in the particles approaches S* (horizontal line), a critical fraction of particles is assumed to crack and macroscopic fracture takes place, as indicated by the crosses in the matrix flow curves.

Application of this approach to describe the fracture behaviour of Al-Si-Cu-Mg casting alloys involves several assumptions: (i) the cracking of eutectic Si, as well as Fe or Cu-rich particles, controls the ductility of the material; (ii) fracture occurs when a critical fraction of particles crack; (iii) the critical fraction of cracked particles to cause fracture is the same for all alloys; (iv) the critical fraction of cracked particles is reached whenever the average stress in the particles, σ_p, approaches a critical value S*, which is of the order of 2–3 times the yield strength[67] of the alloys (≈ 900 MPa); (iv) The volume fraction of reinforcing particles is constant at about 7% for all alloys.

Fig. C-2 shows the ductility and strength of the alloy for a range of S*-values. The calculated values (symbols) are compared with the iso-q lines obtained with Eq. B5. By making the particles more susceptible to fracture by stepwise decreasing S*, sets of symbols are generated which reproduce the pattern of lines of the quality index chart. Physically, a lower S*can be understood as equivalent to having larger Si particles or β-phase platelets. Notice that the symbols shift to the left of the corresponding iso-q lines for decreasing S*-values and increasing proof stress. This implies that an increasing loss in quality index should be expected as the material strength is increased, e.g., through increased Cu or Mg content. Note that the volume fraction of reinforcing particles will also increase with increased Cu or Mg content, so the effect will be magnified. Comparison with actual experimental results is made in Fig. 6.

A similar procedure can be used to incorporate[64] the matrix flow properties and the effects of particle cracking into the equations of the quality index by solving Eq. C2 for s_f, and using this value in Eqs. B5 and B8 to express Q as a function of the matrix parameters K and n and the particle fracture strength S*. The dependence of Q on K is shown by the three solid lines of Fig. 9 (for S* = 875 MPa and given n-values). It is seen that Q goes through a mild maximum for large n, while for decreasing n the maximum becomes increasingly sharper, the Q-value falling rapidly at high values of K.

(Received 19 July 2002, accepted 12 November 2002)